AAAS
Research
Volume 2020, Article ID 5016564, 10 pages
https://doi.org/10.34133/2020/5016564

Research
A SCIENCE PARTNER JOURNAL

Research Article

Achieving High Thermoelectric Performance in Rare-Earth Element-Free $CaMg_2Bi_2$ with High Carrier Mobility and Ultralow Lattice Thermal Conductivity

Muchun Guo,[1] Fengkai Guo,[1] Jianbo Zhu,[1] Li Yin,[2] Qian Zhang,[2] Wei Cai,[1] and Jiehe Sui[1]

[1]*National Key Laboratory for Precision Hot Processing of Metals, Harbin Institute of Technology, Harbin 150001, China*
[2]*Department of Materials Science and Engineering, Harbin Institute of Technology, Shenzhen, Guangdong 518055, China*

Correspondence should be addressed to Jiehe Sui; suijiehe@hit.edu.cn

Received 5 March 2020; Accepted 9 July 2020; Published 24 July 2020

Copyright © 2020 Muchun Guo et al. Exclusive Licensee Science and Technology Review Publishing House. Distributed under a Creative Commons Attribution License (CC BY 4.0).

$CaMg_2Bi_2$-based compounds, a kind of the representative compounds of Zintl phases, have uniquely inherent layered structure and hence are considered to be potential thermoelectric materials. Generally, alloying is a traditional and effective way to reduce the lattice thermal conductivity through the mass and strain field fluctuation between host and guest atoms. The cation sites have very few contributions to the band structure around the fermi level; thus, cation substitution may have negligible influence on the electric transport properties. What is more, widespread application of thermoelectric materials not only desires high ZT value but also calls for low-cost and environmentally benign constituent elements. Here, Ba substitution on cation site achieves a sharp reduction in lattice thermal conductivity through enhanced point defects scattering without the obvious sacrifice of high carrier mobility, and thus improves thermoelectric properties. Then, by combining further enhanced phonon scattering caused by isoelectronic substitution of Zn on the Mg site, an extraordinarily low lattice thermal conductivity of 0.51 $W\,m^{-1}\,K^{-1}$ at 873 K is achieved in $(Ca_{0.75}Ba_{0.25})_{0.995}Na_{0.005}Mg_{1.95}Zn_{0.05}Bi_{1.98}$ alloy, approaching the amorphous limit. Such maintenance of high mobility and realization of ultralow lattice thermal conductivity synergistically result in broadly improvement of the quality factor β. Finally, a maximum ZT of 1.25 at 873 K and the corresponding ZT_{ave} up to 0.85 from 300 K to 873 K have been obtained for the same composition, meanwhile possessing temperature independent compatibility factor. To our knowledge, the current ZT_{ave} exceeds all the reported values in AMg_2Bi_2-based compounds so far. Furthermore, the low-cost and environment-friendly characteristic plus excellent thermoelectric performance also make the present Zintl phase $CaMg_2Bi_2$ more competitive in practical application.

1. Introduction

The development of clean energy could help to alleviate the energy crisis [1, 2]. Recently, solid-state thermoelectric (TE) technology has received a great deal of attention because of its ability to directly convert the waste heat into desirable electricity [3]. The conversion efficiency of thermoelectric device is determined by the dimensionless figure-of-merit $ZT = S^2\sigma T/(\kappa_E + \kappa_L)$, in which S, T, σ, κ_E, and κ_L are Seebeck coefficient, absolute temperature, electrical conductivity, electronic thermal conductivity, and lattice thermal conductivity, respectively [4]. However, the intertwined correlation among the S, σ, and κ_E hinders the further enhancement of ZT value. Thus, some concepts and strategies including band convergence [5, 6], band nestification [7], resonant level [8, 9], and energy filtering [10, 11] have been successfully adopted to optimize the electrical transport properties. On the other hand, progresses on reducing the lattice thermal conductivity κ_L, the sole independent parameter, are also achieved by introducing nanostructuring [12, 13], point defect [14–16], dislocation [17, 18], lattice anharmonicity [19, 20], as well as liquid-like phonons [21, 22] or exploring materials with complex crystal structure [23–25].

Zintl phases seem congenital thermoelectric materials for their structural complexity and inherently low thermal conductivity [26, 27]. Some representative compounds, including

$Yb_{14}MnSb_{11}$ [28], $Ca_{1-x}Yb_xZn_2Sb_2$ [29], Mg_3Sb_2 [30], β-Zn_4Sb_3 [31], $Ca_9Zn_4Sb_9$ [32], and $(Eu_{0.5}Yb_{0.5})_{1-x}Ca_xMg_2Bi_2$ [33], have been exploited for their prominent thermoelectric performance. Particularly, the p-type AM_2X_2 (1-2-2 type) compounds with $CaAl_2Si_2$-type structure deserve intensive attention because of their higher carrier mobility originated from unique crystal structure, where the covalently bonded anionic sheets $(M_2X_2)^{2-}$ sandwiched between A^{2+} cations planes (A contains alkaline earth or divalent rare earth element, M is transition metal or main-group element, X comes from element Sb or Bi) [34]. As one of the two major categories of 1-2-2 type materials, Sb-based system has been paid lots of attention and is in-depth studied. However, it is a pity that the toxic element Cd is always inevitable among Sb-based materials with maximal ZT in excess of 1 [35–39], which is not in keeping with the concept of environmental friendliness. Out of the environmental consideration, peoples gradually turn their concerns to the analogous Bi-based Zintl materials, AMg_2Bi_2 (A = Ca, Yb, Eu) [40, 41].

In the Bi-based family, $CaMg_2Bi_2$ compound possesses the virtues of environmental friendliness, low cost, and high element abundance compared with the other two containing expensive Yb and Eu. Early studies reported that the peak ZT is only ~0.1 for $CaMg_2Bi_2$ synthesized by the traditional melting method, which is far from practical application [41]. Shuai et al. utilized the ball milling method to reduce the element volatilization and then selected the monovalence Na^+ to replace Ca^{2+}, which eventually causes a mediocre $ZT \approx 0.9$ at 873 K for $Ca_{0.995}Na_{0.005}Mg_2Bi_{1.98}$ sample [42]. However, the trace alloying fractions of alkali-metal and weak mass/size difference between alkali-metal and Ca have a faint influence on the lattice thermal conductivity [42]. Attempts at introducing point defect and utilizing multiscale phonon engineering in $CaMg_2Bi_2$ have been executed to further reduce the κ_L [33, 43]. Even though the peak ZT value as high as ~1.3 at 873 K in $Ca_{0.6}Yb_{0.2}Eu_{0.2}Mg_2Bi_2$ is obtained, the expensiveness of some rare-earth elements makes it difficult to achieve large scale application in some cases [33].

In other doped $CaMg_2Bi_2$ systems, the element Ba has been verified to be as effective as Yb or Eu in reducing κ_L [44]. Further considering that Bi-p orbitals dominate the valence band of $CaMg_2Bi_2$ [33], element doping on Ca site may have a minor effect on valence band structure, which is benefited for maintaining high carrier mobility. Thus, starting with the adjusted composition, $Ca_{0.995}Na_{0.005}Mg_2Bi_{1.98}$ [42], the substitution of isoelectronic Ba for Ca will not only tailors carrier concentration while maintaining the high carrier mobility but also reduces the κ_L by constructing point defects, leading to an enhanced thermoelectric properties. Subsequently, Zn doping on Mg site is carried out to further reduce the κ_L. This equivalent substitution can effectively block phonon transmission without significantly disordering the electrical property. Eventually, the maximum ZT value of ~1.25 at 873 K and the average ZT (ZT_{ave}) of ~0.85 between 300 K and 873 K are gained in $(Ca_{0.75}Ba_{0.25})_{0.995}$-$Na_{0.005}Mg_{1.95}Zn_{0.05}Bi_{1.98}$ sample. As well, this ZT_{ave} is the highest value in p-type AM_2X_2 Zintl compounds ever reported, and the richness and nontoxic constituent elements are of great practical significance to promote the application of large-scale and high-efficiency thermoelectric modules.

2. Result and Discussion

2.1. The Effect of Ba Doping on Enhancing TE Properties. The details of sample preparation and characterization could be found in supporting information. Figure 1 shows the XRD patterns and the related lattice parameters of Bax ($x = 0, 0.25, 0.5, 0.75$) alloys. The diffraction peaks can be nicely indexed to trigonal $CaAl_2Si_2$ structure with the space group $P\bar{3}m1$. There is minor impurity phase Bi existing between 25° and 30° on account of the loss of Ca and Mg at elevated temperature. However, it should be noted that the Bragg peaks shift toward lower diffraction angles with increasing Ba fraction as shown in Figure 1(b), indicating an enlarged lattice parameter derived from the larger ionic radius of Ba^{2+} (1.35 Å) compared to that of Ca^{2+} (1.0 Å). As anticipated, the calculated lattice parameters a and c linearly increase with increasing Ba content as shown Figure 1(c).

Figure 2 depicts the electrical transport properties of Bax ($x = 0, 0.25, 0.5, 0.75$) alloys. The decreasing trend of σ as temperature increasing represents a typical degenerate semiconducting behavior. Moreover, the electrical conductivity decreases with increasing Ba content during the whole measured temperature range, which could be attributed to the decrease of carrier concentration since the mobility changes slightly with the doping fraction grows as shown in Figure 2(b) and Table S1.

To further disclose the electrical transport mechanism after doping, the n_H and μ_H as a function of temperature for BaxZny alloys ($x = 0, 0.25, 0.5, 0.75$; $y = 0, 0.05, 0.1, 0.15$) are shown in Figure 2(b). Although Ba and Ca have the same valence state in the Zintl phase, the difference of electronegativity might give rise to diverse electrical properties. The electron transfer may become more distinct in Ba-doped sample because of the higher electropositive of Ba than Ca, which eventually leads to the lower n_H of Ba-doped samples. The similar phenomenon also appears in $Ca_{1-x}Yb_xMg_2Bi_2$ [43] and $Yb_{1-x}Ca_xZn_2Sb_2$ materials [45]. Thus, utilizing the difference of electronegativity does effectively tailor the n_H, which is a crucial approach to modulate the S and σ. Worthy of extraordinary attention here is the independence between carrier mobility and Ba doping fraction. The substitution of cation sites may generate minimal impact on the valence band as mentioned above, and thus, the carrier mobility is nearly unchanged with doping content [33]. Compared with other high-performance $CaMg_2Bi_2$ materials [33, 42–44], we found that this cation doping will not destroy the inherent high mobility of $CaMg_2Bi_2$ system, which is critical in developing high thermoelectric performance (Figure S1). A rough $\mu_H \sim T^{-1.5}$ relationship reveals that the primary carrier scattering mechanism is acoustic phonon scattering (Figure 2(b)).

Figure 2(c) indicates the temperature-dependent Seebeck coefficient of Bax ($x = 0, 0.25, 0.5, 0.75$) alloys. Clearly, the S value increases with increasing Ba fraction, which results from the decreased n_H. Figure 2(d) further shows the

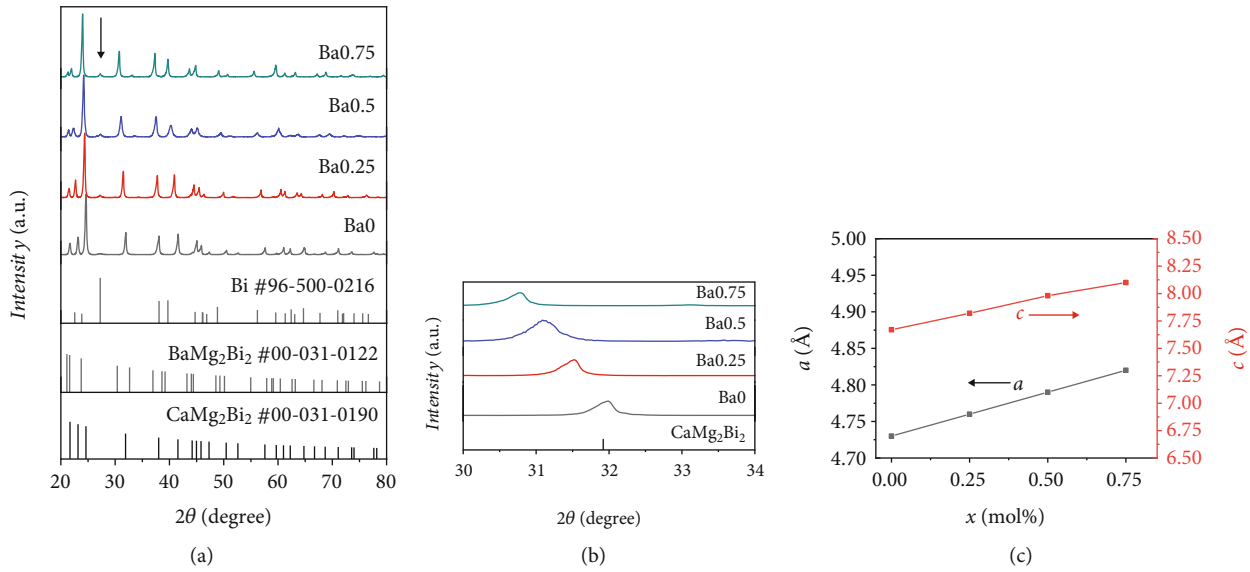


FIGURE 1: (a) The room-temperature XRD patterns for Bax ($x = 0, 0.25, 0.5, 0.75$) alloys. (b) The zoomed-in XRD patterns between 30° and 34°. (c) Ba concentration-dependent lattice parameters.

calculated Pisarenko relations with $m^* = 0.63\, m_e$ at room temperature under the assumption of a parabolic band and an acoustic phonon scattering [46]. The better consistency between the fitting line and experiment data demonstrates that the Ba substitution barely disturbs the valence band structure at room temperature. Although Ba-doping evidently improves the S, the decay of the σ eventually leads to the decline of PF (Figure 2(e)). Even so, the PF value still remains relatively high in Ba0.25 sample and the PF_{ave} of 13.9 μW cm^{-1} K^{-2} ranging from 300 K to 873 K is higher than those of other reports [33, 42, 43] (Figure 3(b)).

At the same time, the power factor dependence on carrier concentration at different temperature is plotted in Figure 2(f). The solid lines represent the calculated PF on the basis of the assumption that the carrier mobility is independent of n_H (Figure 2(b) and Table S1). It is clear that the peak PF can be achieved via adjusting the n_H and the experimental data match well with the calculated PF. Particularly, the optimized carrier concentration at room temperature by calculation is around 2.6×10^{19} cm^{-3}, approximating to the experimental value $\sim 2.5 \times 10^{19}$ cm^{-3} for Ba0.25 sample (Table S1).

Alloying with Ba could substantially decrease the thermal conductivity as shown in Figure 4. The κ_L could be estimated by subtracting electronic component, $\kappa_E = L\sigma T$, from the thermal conductivity κ, in which the Lorenz factor (L) is determined by SPB model assuming the carriers scattering dominated by acoustic phonon. [46] As shown in Figure 4(a), the lattice thermal conductivity first declines with x, reaching the minimum value at $x = 0.5$, and then increases. It should be stressed that the room temperature κ_L reaches a lowest value of 1.1 W m^{-1} K^{-1} for Ba0.5 sample, which is 57% lower than that of undoped sample (2.6 W m^{-1} K^{-1}). Such low κ_L is mainly due to additional phonon scattering results from point defect caused by the mass and strain field fluctuation between doping atoms (Ba) and host atoms (Ca). Under the hypothesis that the phonon propagation is only restricted by Umklapp process and point defect scattering, the Debye-Callaway model [47, 48] has been used to successfully fit the experimentally measured κ_L in diverse systems, such as $YbZn_2Sb_{2-x}Bi_x$ [49], $CaZn_{2-x}Mg_xSb_2$ [50], and $CoSbS_{1-x}Se_x$ [51]. Thus, to deeply clarify the relationship between point defect and the lattice thermal conductivity, the Debye-Callaway model [47, 48] assuming that the phonon scattering mainly comes from contributions of the Umklapp process and point defect scattering terms is adopted in Bax ($x = 0, 0.25, 0.5, 0.75$) materials. A systematic description about the model can be found in supporting information. The parameter Γ presents the strength of point defect scattering and is regarded as a product of the multiplication of Γ_0 and $x_i(1 - x_i)$, where Γ_0 is a dimensionless parameter obtained utilizing a fitting method and x_i is the fractional concentration. The strength of point defect scattering first increases with increasing Ba fraction until $x = 0.5$ and then decreases (Table S2). The minimal κ_L in the $x = 0.5$ sample mainly attributing to maximal lattice disorder. Furthermore, Figure 4(b) shows a good coincidence between model prediction and measured data, which suggests that Ba/Ca substitution are indeed mainly responsible for the reducing of κ_L in this work.

Combined with the reduced κ_E which is proportional to electrical conductivity, the total thermal conductivity sharply decreases as shown in Figures S2 and 4(c). Specially, the room temperature κ decreases from 3.1 W m^{-1} K^{-1} for Ba0 sample to 1.3 W m^{-1} K^{-1} for Ba0.5 sample, with a drop of 58%. Correspondingly, the κ at 873 K reduces from 1.2 W m^{-1} K^{-1} to 0.9 W m^{-1} K^{-1}, with a decrease of 25%. The ZT values as a function of temperature for Bax ($x = 0, 0.25, 0.5, 0.75$) samples are presented in Figure 4(d). Benefiting from the decreased lattice thermal conductivity and appreciable power factor, the maximum ZT value of 1.2 at 823 K is obtained for Ba0.25 alloy.

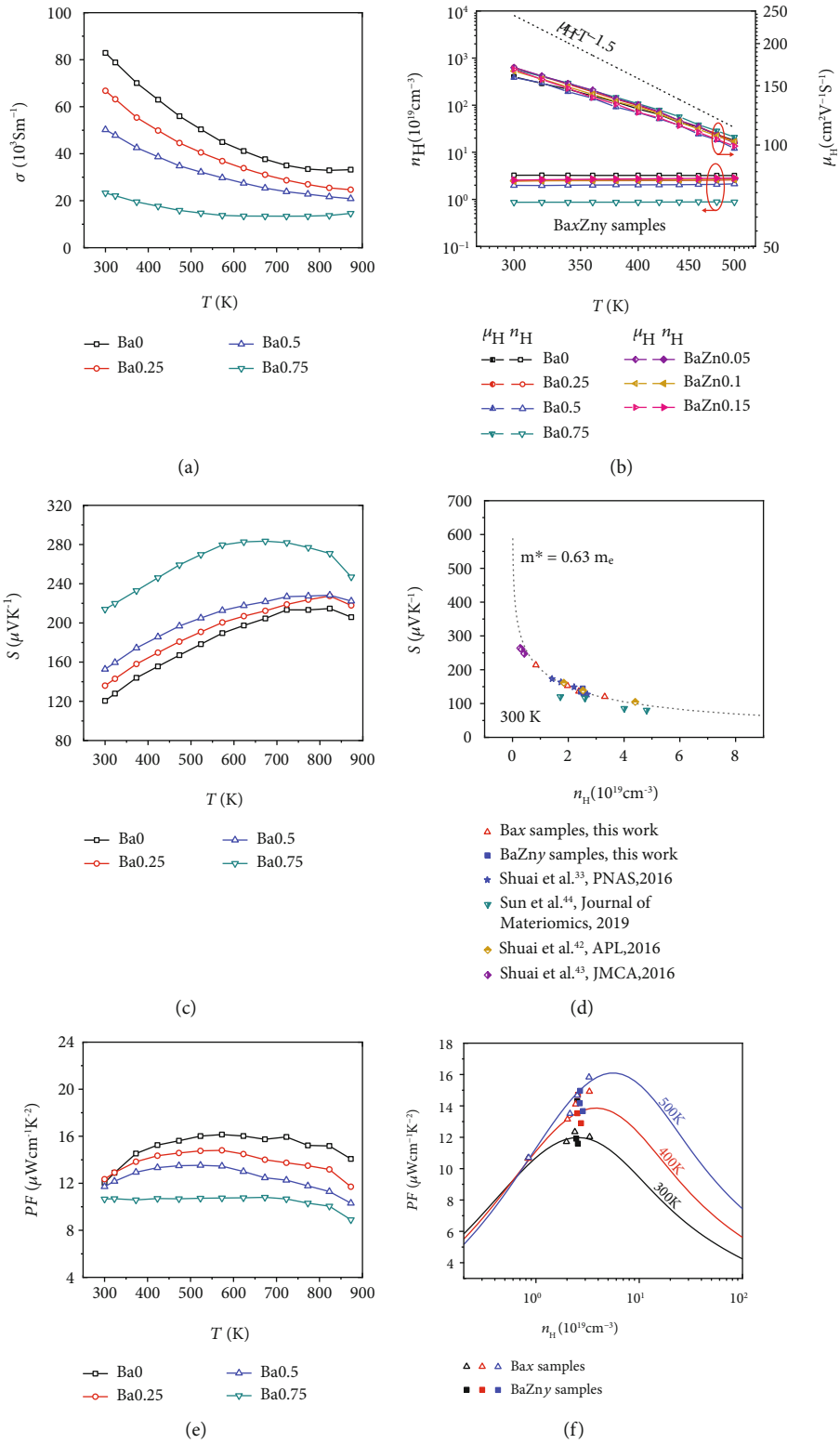


FIGURE 2: (a) The electrical conductivity as a function of temperature for Bax ($x = 0, 0.25, 0.5, 0.75$) samples. (b) Temperature-dependent carrier concentration and mobility for BaxZny ($x = 0, 0.25, 0.5, 0.75$; $y = 0, 0.05, 0.1, 0.15$). The dotted line represents the relationship of μ_H ~$T^{-1.5}$. (c) Temperature-dependent Seebeck coefficient for Bax samples. (d) Room temperature Seebeck coefficient *vs* carrier concentration for our work and the previously reported data [33, 42–44], where the black curve is calculated Pisarenko plot with $m^* = 0.63\, m_e$. (e) Variation of the *PF* for Bax samples. (f) Carrier concentration dependent *PF* at different temperatures. The solid lines are calculated based on SPB with the hypothesis of the insensitive μ_H to carrier concentration. The fitting μ_H values are 164, 130, and 102 $cm^2 V^{-1} s^{-1}$ at 300 K, 400 K, and 500 K, respectively.

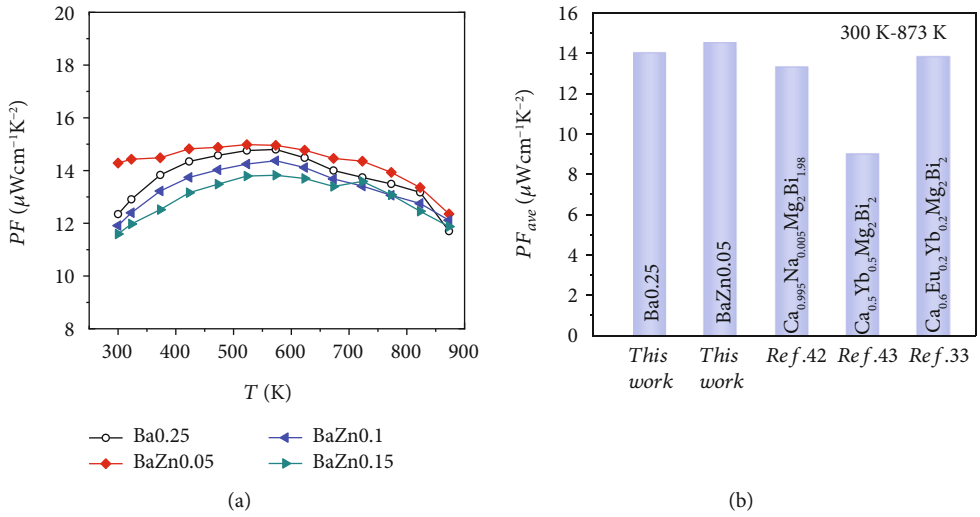


Figure 3: (a) Temperature-dependent PF for BaZny ($y = 0, 0.05, 0.1, 0.15$) samples. (b) Comparison of PF_{ave} for this work with other previous works [33, 42, 43].

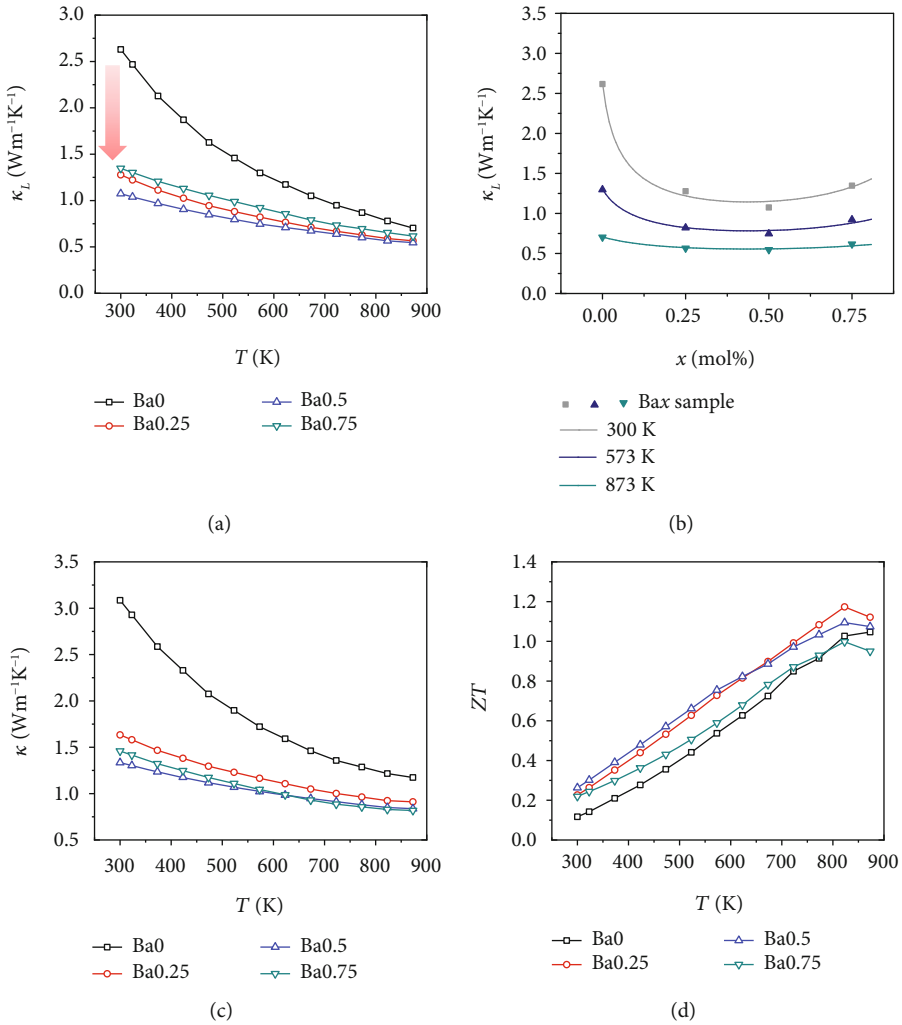


Figure 4: (a) The relationship of κ_L versus temperature for Bax ($x = 0, 0.25, 0.5, 0.75$). (b) Composition dependent lattice thermal conductivity at different temperature with a comparison to model predictions. (c) Temperature dependent thermal conductivity and (d) ZT values of Bax samples.

Table 1: Room temperature electrical transport parameters of BaZny ($y = 0, 0.05, 0.1, 0.15$) samples.

Sample number	Composition	n_H (10^{19} cm^{-3})	μ_H (cm^{-2}V^{-1}s^{-1})	m^* (m_e)	σ (10^3 Sm^{-1})	S (μVK^{-1})
Ba0.25	$(Ca_{0.75}Ba_{0.25})_{0.995}Na_{0.005}Mg_2Bi_{1.98}$	2.5	169	0.63	66.8	136
BaZn0.05	$(Ca_{0.75}Ba_{0.25})_{0.995}Na_{0.005}Mg_{1.95}Zn_{0.05}Bi_{1.98}$	2.5	170	0.66	68.6	144
BaZn0.1	$(Ca_{0.75}Ba_{0.25})_{0.995}Na_{0.005}Mg1.9Zn0.1Bi_{1.98}$	2.5	166	0.62	65.3	135
BaZn0.15	$(Ca_{0.75}Ba_{0.25})_{0.995}Na_{0.005}Mg1.85Zn0.15Bi_{1.98}$	2.5	168	0.61	68.4	130

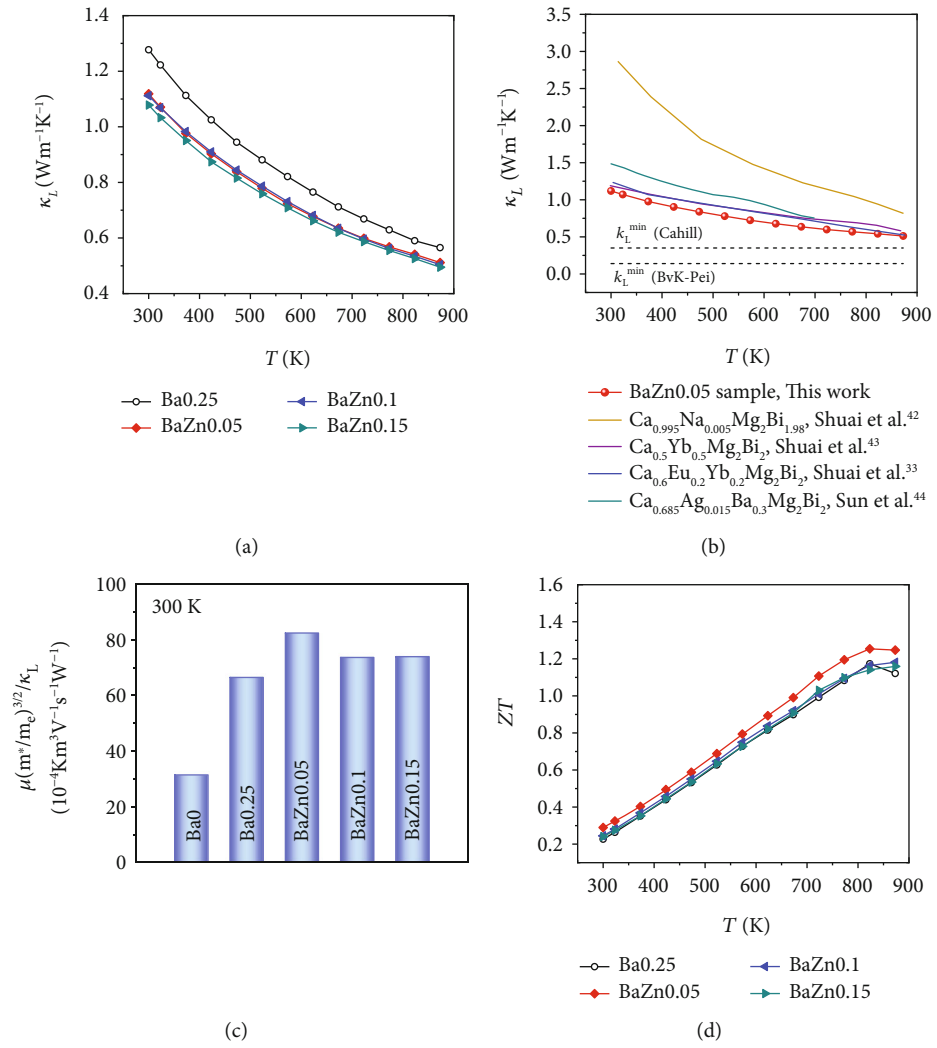


Figure 5: (a) Temperature-dependent the lattice thermal conductivity of BaZny ($y = 0, 0.05, 0.1, 0.15$) samples. (b) Comparison of κ_L between this work and other reported literature [33, 42–44]. The dotted lines represent the theoretical minimum lattice thermal conductivity κ_L^{min} (0.35 W m^{-1} K^{-1} for Cahill model and 0.14 W m^{-1} K^{-1} for Bvk-Pei model) [44]. (c) Composition dependent $\mu(m^*/me)^{3/2}/\kappa_L$ at 300 K for Bax ($x = 0, 0.25$) and BaZny ($y = 0, 0.05, 0.1, 0.15$) samples. (d) The dimensionless figure of merit ZT as a function of temperature and content.

2.2. Mg Site Doping and Its Effect on Enhancing TE Properties. Though the κ_L reaches 0.57 W m^{-1} K^{-1} at 873 K for Ba0.25 sample, this value is still much higher than the theoretical limit (0.35 W m^{-1} K^{-1} for Cahill model and 0.14 W m^{-1} K^{-1} for Bvk-Pei model) [44]. How to further decrease κ_L while maintaining the considerable PF is another urgent challenge. One of the interesting characteristics of isoelectronic alloying is that they do not bring the charge disorder but introduce the phonon scattering center due to the mass and strain field fluctuations between the host atoms and the guest atoms [52]. In our previous work, we have confirmed firstly that Zn substitution on Mg site can reduce the κ_L without changing the valence band structure [53]. Thus, lower lattice thermal conductivity is prospected in properly BaZny alloys, which is advantageous for enhancing ZT values.

Room temperature XRD analysis of BaZny ($y = 0, 0.05, 0.1, 0.15$) samples is displayed in Figure S3. Besides tiny Bi impurity, the main phases of all samples

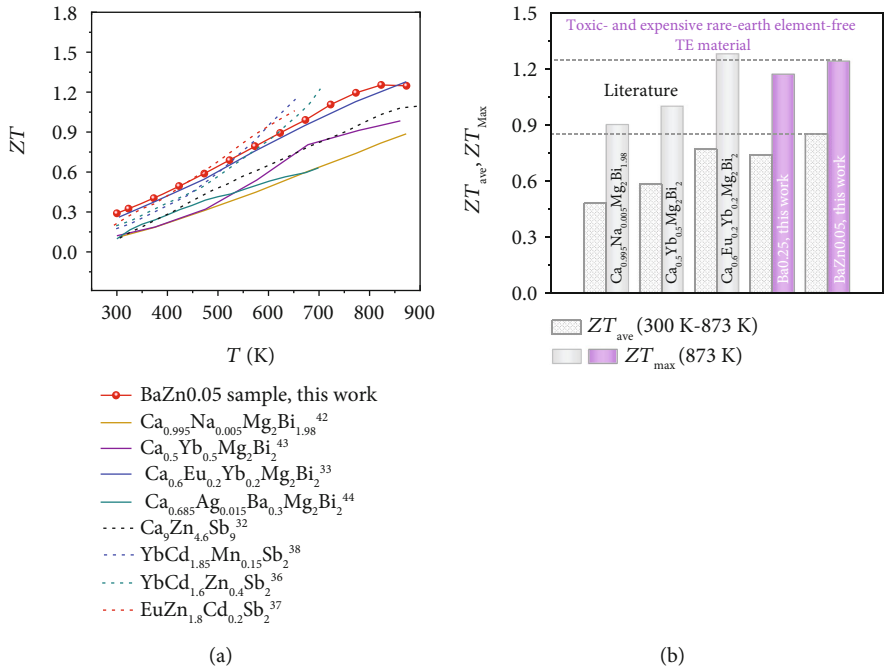


FIGURE 6: (a) Comparison of ZT values between BaZn0.05 sample and other reported samples in p-type AM_2X_2 Zintls [32, 33, 36–38, 42–44]. (b) The maximal ZT_{max} (873 K) and ZT_{ave} (300 K-873 K) between this work and other previous $CaMg_2Bi_2$ alloys [33, 42, 43].

exhibit good agreement with the $CaAl_2Si_2$ structure (space group $P\ \bar{3}\ m1$). It is noted that the lattice parameter increases with Zn content grows up due to the small ionic radius of Zn in comparison with Mg. However, no distinct deviations occur in lattice constant when y exceeds 0.05, which can be attributed to the low solubility limit of Zn in the present compound.

Figure S4 shows temperature-dependent σ and S for BaZny ($y = 0, 0.05, 0.1, 0.15$). The slightly variation in the electrical conductivity with increasing Zn fraction can be explained by the almost unchanged carrier concentration and mobility (Figure 2(b) and Table 1). Zn doping has a faint effect on the Seebeck coefficient when $y \leq 0.05$, and the Seebeck coefficients present a downward trend when doping concentration exceed 0.05. The reason for the decline of S is still unclear and need further research. One possible explanation is that Zn-related second phase influences the Seebeck coefficient in some degree. As shown in Table 1 and Figure 2(d), the m^* is less influenced by doping and all experimental data fall well on the Pisarenko curve, indicating that Zn doping has a tiny influence on the valence band structure at 300 K. In previous literature of the same group [53], it is founded that the carrier mobility of $CaMg_{1.8}Zn_{0.2}Bi_{1.98}$ decreases with a drop of 20% compared to $CaMg_2Bi_{1.98}$. However, the carrier mobility is reduced by less than 10% when the Zn doping fraction is less than 0.05. It is generally recognized that the carrier mobility increases with the decrease of carrier concentration. However, in this work, Ba doping reduced carrier concentration, but the carrier mobility remained nearly unchanged rather than increased, further indicating that the alloying scattering caused by Ba doping has a certain effect on the mobility reduction. When we further dope slight Zn (Zn = 0.05) in $(Ca_{0.75}Ba_{0.25})_{0.995}Na_{0.005}Mg_2Bi_{1.98}$, its weak carrier scattering effect could be obscured by that caused by Ba doping in $(Ca_{0.75}Ba_{0.25})_{0.995}Na_{0.005}Mg_2Bi_{1.98}$, leading to an inconspicuous change on mobility. Moreover, the experimental carrier concentration of $\sim 2.5 \times 10^{19}\ cm^{-3}$ for Zn-doped samples is close to the optimal range for maximum PF, as shown in Figure 2(f). The high carrier mobility of $\sim 164\ cm^{-2}\ V^{-1}\ s^{-1}$ is still at a higher level, even compared with other doped $CaMg_2Bi_2$ [33, 42–44], as shown in Figure S1.

With increasing Zn content, the PF of BaZny samples increases firstly when $y \leq 0.05$ and then decreases (Figure 3(a)). A conclusion that the appropriate Zn concentration will not deteriorate the electrical transport properties can be made. It is known that the output power density (ω) is proportional to the power factor via $\omega = 1/4((T_h - T_c)^2/L)PF$ [54]. Thus, the highest PF_{ave} of $14.4\ \mu W\ cm^{-1}\ K^{-2}$ in BaZn0.05 sample contributes to a higher output power density compared with the other representative reports [33, 42, 43].

Further investigation on thermal transport parameters is carried out. Alloying Zn in Ba0.25 sample indeed effectively reduces the κ_L throughout the measured temperature range due to the enhanced point defects scattering (as shown in Figure 5(a)). The κ_L decreases from $\sim 1.3\ W\ m^{-1}\ K^{-1}$ for Ba0.25 sample to $1.1\ W\ m^{-1}\ K^{-1}$ BaZn0.05 sample at 300 K and from $0.6\ W\ m^{-1}\ K^{-1}$ to $0.5\ W\ m^{-1}\ K^{-1}$ at 873 K, which are definitely lower than those of other reported $CaMg_2Bi_2$ systems [33, 42–44] (Figure 5(b)). Specially, the lower κ_L of $0.5\ W\ m^{-1}\ K^{-1}$ in this work approaches to the amorphous limit κ_L^{min} as shown Figure 5(b) [44], originating from the high concentration point defects caused by Ba and Zn

alloying. The reduced lattice thermal conductivity eventually leads to the decline of total thermal conductivity, as shown in Figure S5.

In general, for the intrinsic materials metric, quality factor β ($\mu(m^*/me)^{3/2}/\kappa_L$) was taken as reference to search potential thermoelectric materials [55]. The room temperature β of BaxZny ($x = 0, 0.25$, $y = 0, 0.05, 0.1, 0.15$) is plotted in Figure 5(c). A largest value of 82.4×10^{-4} K m^3 V^{-1} s^{-1} W^{-1} is achieved in the $x = 0.25$, $y = 0.05$ samples, which is about two times higher than that of the Ba0 sample (31.4×10^{-4} K m^3 V^{-1} s^{-1} W^{-1}). Thus, with the help of Ba and Zn dual doping, we could realize reduced lattice thermal conductivity without serious compromises in electrical properties. As shown in Figure 5(d), the highest ZT value of ~1.25 is achieved for BaZn0.05 sample when it is higher than 823 K.

Snyder and Ursell [56] proposes that the compatibility factor $s = (\sqrt{1 + ZT} - 1)/(ST)$ can be used to facilitate rational materials selection and thermoelectric device design. An optimal relative current density is essential for achieving the maximum conversion efficiency. However, for the segmented power generation modules containing different materials, the electric current flowing in each part should be the same. Thus, the maximum conversion efficiency of each part could be achieved if the compatibility factor of one segment is similar to one another [56]. The situation that a single leg made of a single material is applied within a temperature gradient can be analogous to the different-material segments mentioned above. Each part of such a segment in different temperature may not be capable of achieving the largest conversion efficiency together unless the compatibility factor is independent of temperature. Figure S6 shows that the compatibility factor of Ba and Zn doping are almost temperature independence, which is conducive to maximize efficiency in the whole application temperature range.

Compared to other doped $CaMg_2Bi_2$ compounds [33, 42–44], the ZT value of 1.25 for BaZn0.05 sample catches up with the current highest level, as shown in Figure 6(a). Besides the appreciable ZT, a record ZT_{ave} of 0.85 is also achieved for the same materials system (Figure 6(b)). The relatively cost-effective, nontoxic, and abundant constituents combined with the high thermoelectric performance makes the present compound more attractive among all thermoelectric material systems.

3. Conclusion

In this work, p-type $CaMg_2Bi_2$ was transformed from an uncompetitive thermoelectric material to an outstanding one with record ZT_{ave} via Ba and Zn dual doping. High-concentration point defects (Ba and Zn doping) play a crucial role in obstructing phonon transport due to the large mass and size difference between the host atom and guest atom. An ultralow κ_L of 0.51 W m^{-1} K^{-1} at 873 K is obtained for $(Ca_{0.75}Ba_{0.25})_{0.995}Na_{0.005}Mg_{1.95}Zn_{0.05}Bi_{1.98}$ sample. Further, due to the weakly affected carrier mobility, the quality factor β will be distinctly strengthened. Eventually, the enhanced ZT_{max} of 1.25 at 873 K and the record ZT_{ave} of 0.85 between 300 K and 873 K are also obtained. Last but not least, just this material also displays the temperature independent compatibility factor. Taking into account the practical design of thermoelectric device, high-performance thermoelectric materials composed of cost-effective, environmentally friendly, and plentiful elements are of greatly practical significance for large-scale commercial applications.

Conflicts of Interest

The authors declare no conflict of interest.

Authors' Contributions

M. Guo, F. Guo, and J. Sui designed the experiment; M. Guo and F. Guo performed the synthesis and thermoelectric property measurement; J. Zhu and L. Yin conducted the lattice thermal calculation and Hall measurement; M. Guo, F. Guo, J. Zhu, Q. Zhang, W. Cai, and J. Sui analyzed data and discussed the results. M. Guo, F. Guo, and J. Sui complete the writing of manuscript. M. Guo and F. Guo contributed equally to this manuscript.

Acknowledgments

This work was supported by the National Natural Science Foundation of China (Nos. 51771065 and 51871082).

Supplementary Materials

Experimental Section: sample preparation and sample characterization. Figure S1: carrier mobility *vs* carrier concentration between this work and other literature of $CaMg_2Bi_2$ materials. Figure S2: temperature-dependent the electronic thermal conductivity of Bax ($x = 0, 0.25, 0.5, 0.75$) samples. Figure S3: (a) the XRD patterns of BaZny ($y = 0, 0.05, 0.1, 0.15$). (b) Enlarged view of XRD patterns between 35° and 39°. (c) Lattice constant as a function of composition. Figure S4: temperature-dependent (a) the electrical conductivity and (b) the Seebeck coefficient of BaZny ($y = 0, 0.05, 0.1, 0.15$). Figure S5: the thermal conductivity as a function of temperature for BaZny ($y = 0, 0.05, 0.1, 0.15$). Figure S6: the compatibility factors *vs* temperature for Bax ($x = 0, 0.25$) and BaZny ($y = 0.05, 0.1, 0.15$) sample. Table S1: room temperature electrical transport parameters of Bax ($x = 0, 0.25, 0.5, 0.75$). Calculation of lattice thermal conductivity using the Callaway Model. *(Supplementary Materials)*

References

[1] T. Sun, Z. J. Li, and X. B. Zhang, "Achieving of High Density/Utilization of Active Groups via Synergic Integration of C=N and C=O Bonds for Ultra-Stable and High-Rate Lithium-Ion Batteries," *Research*, vol. 2018, article 1936735, pp. 1–10, 2018.

[2] L. L. Baranowski, G. J. Snyder, and E. S. Toberer, "Concentrated solar thermoelectric generators," *Energy & Environmental Science*, vol. 5, no. 10, pp. 9055–9067, 2012.

[3] J. Mao, Z. Liu, J. Zhou et al., "Advances in thermoelectrics," *Advances in Physics*, vol. 67, no. 2, pp. 69–147, 2018.

[4] I. T. Witting, F. Ricci, T. C. Chasapis, G. Hautier, and G. J. Snyder, "The Thermoelectric Properties of *n*-Type Bismuth Telluride: Bismuth Selenide Alloys $Bi_2Te_{3-x}Se_x$," *Research*, vol. 2020, article 4361703, pp. 1–15, 2020.

[5] Y. Tang, Z. M. Gibbs, L. A. Agapito et al., "Convergence of multi-valley bands as the electronic origin of high thermoelectric performance in $CoSb_3$ skutterudites," *Nature Materials*, vol. 14, no. 12, pp. 1223–1228, 2015.

[6] Y. Wu, P. Nan, Z. Chen et al., "Manipulation of Band Degeneracy and Lattice Strain for Extraordinary PbTe Thermoelectrics," *Research*, vol. 2020, article 8151059, pp. 1–12, 2020.

[7] S. Lin, W. Li, Z. Chen, J. Shen, B. Ge, and Y. Pei, "Tellurium as a high-performance elemental thermoelectric," *Nature Communications*, vol. 7, no. 1, article 10287, 2016.

[8] J. P. Heremans, V. Jovovic, E. S. Toberer et al., "Enhancement of thermoelectric efficiency in PbTe by distortion of the electronic density of states," *Science*, vol. 321, no. 5888, pp. 554–557, 2008.

[9] Q. Zhang, B. Liao, Y. Lan et al., "High thermoelectric performance by resonant dopant indium in nanostructured SnTe," *Proceedings of the National Academy of Sciences of United States of America*, vol. 110, no. 33, pp. 13261–13266, 2013.

[10] C. Gayner and Y. Amouyal, "Energy filtering of charge carriers: current trends, challenges, and prospects for thermoelectric materials," *Advanced Functional Materials, article*, vol. 30, no. 18, article 1901789, 2020.

[11] J. M. O. Zide, D. Vashase, Z. X. Bian et al., "Demonstration of electron filtering to increase the Seebeck coefficient in $In_{0.53}Ga_{0.47}As/In_{0.53}Ga_{0.28}Al_{0.19}As$ superlattices," *Physical Review B*, vol. 74, no. 20, article 205335, 2006.

[12] C. Zhao, Z. Li, T. Fan, C. Xiao, and Y. Xie, "Defects Engineering with Multiple Dimensions in Thermoelectric Materials," *Research*, vol. 2020, article 9652749, pp. 1–23, 2020.

[13] P. Jood, M. Ohta, A. Yamamoto, and M. G. Kanatzidis, "Excessively doped PbTe with Ge-induced nanostructures enables high-efficiency thermoelectric modules," *Joule*, vol. 2, no. 7, pp. 1339–1355, 2018.

[14] H. Zhang, T. Zheng, B. Gnade, and K. Cho, "The effect of point defects and nanoparticles on thermal conductivity of magnesium silicide," *Computational Materials Science*, vol. 104, pp. 172–176, 2015.

[15] C. Yang, K. Guo, X. Yang et al., "Realizing high thermoelectric performance in $BaCu_{2-x}Ag_xTe_2$ through enhanced carrier effective mass and point-defect scattering," *ACS Applied Energy Materials*, vol. 2, no. 1, pp. 889–895, 2018.

[16] X. Li, P. Yang, Y. Wang et al., "Phase Boundary Mapping in ZrNiSn Half-Heusler for Enhanced Thermoelectric Performance," *Research*, vol. 2020, article 4630948, pp. 1–9, 2020.

[17] Z. Chen, B. Ge, W. Li et al., "Vacancy-induced dislocations within grains for high-performance PbSe thermoelectrics," *Nature Communications*, vol. 8, no. 1, article 13828, 2017.

[18] F. Guo, B. Cui, Y. Liu et al., "Thermoelectric SnTe with Band Convergence, Dense Dislocations, and Interstitials through Sn Self-Compensation and Mn Alloying," *Small*, vol. 14, no. 37, article 1802615, 2018.

[19] S. N. Guin, D. S. Negi, R. Datta, and K. Biswas, "Nanostructuring, carrier engineering and bond anharmonicity synergistically boost the thermoelectric performance of p-type $AgSbSe_2$–ZnSe," *Journal of Materials Chemistry A*, vol. 2, no. 12, pp. 4324–4331, 2014.

[20] G. A. S. Ribeiro, L. Paulatto, R. Bianco, I. Errea, F. Mauri, and M. Calandra, "Strong anharmonicity in the phonon spectra of PbTe and SnTe from first principles," *Physical Review B*, vol. 97, no. 1, article 014306, 2018.

[21] H. Liu, X. Shi, F. Xu et al., "Copper ion liquid-like thermoelectrics," *Nature Materials*, vol. 11, no. 5, pp. 422–425, 2012.

[22] W. Qiu, L. Xi, P. Wei, X. Ke, J. Yang, and W. Zhang, "Part-crystalline part-liquid state and rattling-like thermal damping in materials with chemical-bond hierarchy," *Proceedings of the National Academy of Sciences of the United States of America*, vol. 111, no. 42, pp. 15031–15035, 2014.

[23] S. Roychowdhury, M. K. Jana, J. Pan et al., "Soft phonon modes leading to ultralow thermal conductivity and high thermoelectric performance in AgCuTe," *Angewandte Chemie*, vol. 57, no. 15, pp. 4043–4047, 2018.

[24] H. Lin, G. Tan, J. N. Shen et al., "Concerted rattling in $CsAg_5Te_3$ Leading to ultralow thermal conductivity and high thermoelectric performance," *Angewandte Chemie International Edition*, vol. 55, no. 38, pp. 11431–11436, 2016.

[25] P.-P. Shang, J. Dong, J. Pei et al., "Highly Textured N-Type SnSe Polycrystals with Enhanced Thermoelectric Performance," *Research*, vol. 2019, article 9253132, pp. 1–10, 2019.

[26] J. Shuai, J. Mao, S. Song, Q. Zhang, G. Chen, and Z. Ren, "Recent progress and future challenges on thermoelectric Zintl materials," *Materials Today Physics*, vol. 1, pp. 74–95, 2017.

[27] S. M. Kauzlarich, S. R. Brown, and G. J. Snyder, "Zintl phases for thermoelectric devices," *Dalton Transactions*, no. 21, pp. 2099–2107, 2007.

[28] E. S. Toberer, C. A. Cox, S. R. Brown et al., "Traversing the metal-insulator transition in a Zintl phase: rational enhancement of thermoelectric efficiency in $Yb_{14}Mn_{1-x}Al_xSb_{11}$," *Advanced Functional Materials*, vol. 18, no. 18, pp. 2795–2800, 2008.

[29] F. Gascoin, S. Ottenssmann, D. Stark, S. M. Haïle, and G. J. Snyder, "Zintl phases as thermoelectric materials: tuned transport properties of the compounds $Ca_xYb_{1-x}Zn_2Sb_2$," *Advanced Functional Materials*, vol. 15, no. 11, pp. 1860–1864, 2005.

[30] Z. Han, Z. Gui, Y. B. Zhu et al., "The electronic transport channel protection and tuning in real space to boost the thermoelectric performance of $Mg_{3+\delta}Sb_{2-y}Bi_y$ near room temperature," *Research*, vol. 2020, article 1672051, pp. 1–12, 2020.

[31] M. Chitroub, F. Besse, and H. Scherrer, "Thermoelectric properties of semi-conducting compound Zn_4Sb_3," *Journal of Alloys & Compounds*, vol. 460, no. 1-2, pp. 90–93, 2008.

[32] S. Ohno, U. Aydemir, M. Amsler et al., "Achieving zT > 1 in Inexpensive Zintl Phase Ca_9Zn_{4+x} Sb_9 by Phase Boundary Mapping," *Advanced Functional Materials*, vol. 27, no. 20, article 1606361, 2017.

[33] J. Shuai, H. Geng, Y. Lan et al., "Higher thermoelectric performance of Zintl phases $(Eu_{0.5}Yb_{0.5})_{1-x}Ca_xMg_2Bi_2$ by band engineering and strain fluctuation," *Proceedings of the National Academy of Sciences of the United States of America*, vol. 113, no. 29, pp. E4125–E4132, 2016.

[34] W. Y. Peng, S. Chanakian, and A. Zevalkink, "Crystal chemistry and thermoelectric transport of layered AM_2X_2 compounds," *Inorganic Chemistry Frontiers*, vol. 5, no. 8, pp. 1744–1759, 2018.

[35] X. Wang, J. Li, C. Wang et al., "Orbital alignment for high performance thermoelectric $YbCd_2Sb_2$ Alloys," *Chemistry of Materials*, vol. 30, no. 15, pp. 5339–5345, 2018.

[36] X. Wang, L. W. Guo, H. Q. Jia et al., "Synthesis and high thermoelectric efficiency of Zintl phase $YbCd_{2-x}Zn_xSb_2$," *Applied Physics Letters*, vol. 94, no. 9, article 092106, 2009.

[37] H. Zhang, M. Baitinger, M. B. Tang et al., "Thermoelectric properties of $Eu(Zn_{1-x}Cd_x)_2Sb_2$," *Dalton Transactions*, vol. 39, no. 4, pp. 1101–1104, 2010.

[38] G. Kai, Q.-G. Cao, X.-J. Feng et al., "Enhanced Thermoelectric Figure of Merit of Zintl Phase $YbCd_{2-x}Mn_xSb_2$ by Chemical Substitution," *European Journal of Inorganic Chemistry*, vol. 2011, no. 26, pp. 4043–4048, 2011.

[39] Q. G. Cao, J. Zheng, K. Zhang, and G. Ma, "Thermoelectric properties of $YbCd_2Sb_2$ doped by Mg," *Journal of Alloys and Compounds*, vol. 680, pp. 278–282, 2016.

[40] A. F. May, M. A. McGuire, D. J. Singh, R. Custelcean, and G. E. Jellison Jr., "Structure and properties of single crystalline $CaMg_2Bi_2$, $EuMg_2Bi_2$, and $YbMg_2Bi_2$," *Inorganic Chemistry*, vol. 50, no. 21, pp. 11127–11133, 2011.

[41] A. F. May, M. A. McGuire, D. J. Singh et al., "Thermoelectric transport properties of $CaMg_2Bi_2$, $EuMg_2Bi_2$, and $YbMg_2Bi_2$," *Physical Review B*, vol. 85, no. 3, article 035202, 2012.

[42] J. Shuai, H. S. Kim, Z. Liu, R. He, J. Sui, and Z. Ren, "Thermoelectric properties of Zintl compound $Ca_{1-x}Na_xMg_2Bi_{1.98}$," *Applied Physics Letters*, vol. 108, no. 18, article 183901, 2016.

[43] J. Shuai, Z. H. Liu, H. S. Kim et al., "Thermoelectric properties of Bi-based Zintl compounds $Ca_{1-x}Yb_xMg_2Bi_2$," *Journal of Materials Chemistry A*, vol. 4, no. 11, pp. 4312–4320, 2016.

[44] C. Sun, X. Shi, L. Zheng, B. Chen, and W. Li, "Transport properties of p-type $CaMg_2Bi_2$ thermoelectrics," *Journal of Materiomics*, vol. 5, no. 4, pp. 567–573, 2019.

[45] J. Shuai, Y. Wang, Z. Liu et al., "Enhancement of thermoelectric performance of phase pure Zintl compounds $Ca_{1-x}Yb_xZn_2Sb_2$, $Ca_{1-x}Eu_xZn_2Sb_2$, and $Eu_{1-x}Yb_xZn_2Sb_2$ by mechanical alloying and hot pressing," *Nano Energy*, vol. 25, pp. 136–144, 2016.

[46] H. J. Goldsmid, *Introduction to Thermoelectricity*, Springer, 2010.

[47] J. Callaway and H. C. von Baeyer, "Effect of point imperfections on lattice thermal conductivity," *Physical Review*, vol. 120, no. 4, pp. 1149–1154, 1960.

[48] P. G. Klemens, "Thermal resistance due to point defects at high temperatures," *Physical Review*, vol. 119, no. 2, pp. 507–509, 1960.

[49] X. Zhang, H. Gu, Y. Zhang et al., "Enhanced thermoelectric properties of $YbZn_2Sb_{2-x}Bi_x$ through a synergistic effect via Bi-doping," *Chemical Engineering Journal*, vol. 374, pp. 589–595, 2019.

[50] M. Wood, U. Aydemir, S. Y. Ohno, and G. J. Snyder, "Observation of valence band crossing: the thermoelectric properties of $CaZn_2Sb_2$–$CaMg_2Sb_2$ solid solution," *Journal of Materials Chemistry A*, vol. 6, no. 20, pp. 9437–9444, 2018.

[51] W. Yao, D. Yang, Y. Yan et al., "Synergistic strategy to enhance the thermoelectric properties of $CoSbS_{1-x}Se_x$ Compounds via solid solution," *ACS Applied Materials & Interfaces*, vol. 9, no. 12, pp. 10595–10601, 2017.

[52] J. Yang, G. P. Meisner, and L. Chen, "Strain field fluctuation effects on lattice thermal conductivity of ZrNiSn-based thermoelectric compounds," *Applied Physics Letters*, vol. 85, no. 7, pp. 1140–1142, 2004.

[53] M. C. Guo, F. Guo, J. Zhu et al., "Enhanced thermoelectric properties of p-type $CaMg_2Bi_2$ via a synergistic effect originated from Zn and alkali-metal co-doping," *ACS Applied Materials & Interfaces*, vol. 12, no. 5, pp. 6015–6021, 2020.

[54] W. S. Liu, H. S. Kim, Q. Jie, and Z. F. Ren, "Importance of high power factor in thermoelectric materials for power generation application: a perspective," *Scripta Materialia*, vol. 111, pp. 3–9, 2016.

[55] H. Wang, Y. Z. Pei, A. D. Lalonde, and G. Jeffery Snyder, "Material Design Considerations Based on Thermoelectric Quality Factor," in *Thermoelectric Nanomaterials*, K. Koumoto and T. Mori, Eds., vol. 182 of Springer Series in Materials Science, Springer,, Berlin, Heidelberg, 2013.

[56] G. J. Snyder and T. S. Ursell, "*Thermoelectric Efficiency and Compatibility*," *Physical Review Letters*, vol. 91, no. 14, article 148301, 2003.